

Geochemistry, Geophysics, Geosystems

RESEARCH ARTICLE

10.1029/2018GC007511

Special Section:

Magnetism in the Geosciences
– Advances and Perspectives

Key Points:

- The FORC-PCA unmixing method is tested on synthetic mixtures of magnetic domain states
- A new FORC-PCA algorithm is developed that solves the linear mixing problem for end-members with different domain states (including superparamagnetism)
- Feasibility metrics are developed that help to guide identification of physically realistic end-members

Supporting Information:

- Supporting Information S1
- Data Set S1
- Data Set S2
- Data Set S3
- Data Set S4
- Data Set S5

Correspondence to:

R. J. Harrison,
rjh40@cam.ac.uk

Citation:

Harrison, R. J., Muraszko, J., Heslop, D., Lascu, I., Muxworthy, A. R., & Roberts, A. P. (2018). An improved algorithm for unmixing first-order reversal curve diagrams using principal component analysis. *Geochemistry, Geophysics, Geosystems*, 19, 1595–1610. <https://doi.org/10.1029/2018GC007511>

Received 26 FEB 2018

Accepted 12 APR 2018

Accepted article online 19 APR 2018

Published online 16 MAY 2018

© 2018. American Geophysical Union.
All Rights Reserved.

An Improved Algorithm for Unmixing First-Order Reversal Curve Diagrams Using Principal Component Analysis

Richard J. Harrison¹ , Joy Muraszko¹, David Heslop² , Ioan Lascu³ , Adrian R. Muxworthy⁴, and Andrew P. Roberts² 

¹Department of Earth Sciences, University of Cambridge, Cambridge, UK, ²Research School of Earth Sciences, Australian National University, Canberra, Australian Capital Territory, Australia, ³Department of Mineral Sciences, National Museum of Natural History, Smithsonian Institution, Washington, DC, USA, ⁴Department of Earth Science and Engineering, Imperial College, London, UK

Abstract First-order reversal curve (FORC) diagrams of synthetic binary mixtures with single-domain, vortex state, and multidomain end-members (EMs) were analyzed using principal component analysis (FORC-PCA). Mixing proportions derived from FORC-PCA are shown to deviate systematically from the known weight percent of EMs, which is caused by the lack of reversible magnetization contributions to the FORC distribution. The error in the mixing proportions can be corrected by applying PCA to the raw FORCs, rather than to the processed FORC diagram, thereby capturing both reversible and irreversible contributions to the signal. Here we develop a new practical implementation of the FORC-PCA method that enables quantitative unmixing to be performed routinely on suites of FORC diagrams with up to four distinct EMs. The method provides access not only to the processed FORC diagram of each EM, but also to reconstructed FORCs, which enables objective criteria to be defined that aid identification of physically realistic EMs. We illustrate FORC-PCA with examples of quantitative unmixing of magnetic components that will have widespread applicability in paleomagnetism and environmental magnetism.

1. Introduction

Natural samples contain magnetic minerals with a wide range of grain sizes, domain states, coercivity distributions, anisotropies, and interaction fields. First-order reversal curve (FORC) diagrams provide a powerful method to characterize all these aspects of the magnetic mineralogy (Pike et al., 1999; Roberts et al., 2000, 2014), although their interpretation in the literature is often based on qualitative assessments and empirical “fingerprinting.” Developments in theoretical modeling (Egli, 2006; Harrison & Lascu, 2014; Muxworthy et al., 2004; Newell, 2005; Roberts et al., 2017), new measurement protocols (Zhao et al., 2015, 2017), and new analysis methods (Egli, 2013; Egli & Winklhofer, 2014; Heslop et al., 2014) have placed the processing and interpretation of FORC diagrams onto a firm physical footing, which provides the opportunity for a more quantitative approach to rock magnetic characterization. Application of principal component analysis (Jolliffe, 2002) to analyze entire sets of FORC diagrams (FORC-PCA) was introduced by Lascu et al. (2015) as a quantitative method to unmix a suite of related samples into a linear combination of up to four end-members (EMs). The method has been applied successfully to unmix the biogenic and detrital magnetic components of a sediment core from the Rockall Trough (Channell et al., 2016), to characterize glacial/interglacial sedimentation on the Northwest Iberian Margin (Plaza-Morlote et al., 2017), and to unmix the pedogenic and detrital magnetic components of Minnesotan soils (Maxbauer et al., 2017). The key advantage of FORC-PCA lies in the two-dimensional nature of the FORC diagram. Unmixing one-dimensional coercivity distributions (e.g., by fitting to the sum of standard basis functions) can be ambiguous, especially when there is strong overlap between the coercivity distributions of different components (Heslop, 2015). The information provided by the vertical B_u axis of an FORC diagram, however, provides additional sensitivity to the presence of superparamagnetic (SP), single-domain (SD), vortex (V), and multidomain (MD) states, the ability to detect the presence or absence of interactions in each EM, and a way to discriminate between minerals with different types of magnetocrystalline anisotropy. Note that throughout this paper we follow Roberts et al. (2017) in referring to “vortex” states rather than to “pseudo-single domain” or “PSD” states. The term “vortex” is broadly defined by Roberts et al. (2017) to include both single-vortex (SV) and

multivortex (MV) states, which more accurately describe the physics of magnetic particles (Donnelly et al., 2017) in the intermediate size range between the SD and MD states.

Despite the numerous advantages of FORC-PCA, the method has some shortcomings that currently limit its usefulness for rock magnetic characterization. First, the FORC distribution is sensitive primarily to the irreversible component of the magnetic response of a sample to a changing magnetic field. Purely reversible responses to the changing field (e.g., from superparamagnetic, paramagnetic, antiferromagnetic, or diamagnetic sources), are strictly absent from the FORC diagram, and cannot be identified as EM components in a FORC-PCA analysis. Even for ferrimagnetic sources, the magnetization response of any sample can be split into the sum of reversible and irreversible components, with the ratio of the two depending largely on the domain state: SD states are dominated by irreversible magnetization, whereas MD states are dominated by reversible magnetization. In its current form, therefore, the unmixing proportions reported by FORC-PCA may deviate significantly from the actual proportions (by mass or volume) of the EMs present in the sample, especially if the EMs represent populations of grains with different domain states. Second, the process of choosing appropriate EMs (based often on a limited sampling of the unmixing space by a data set) can be subject to nonuniqueness, user subjectivity, and in the most serious cases, to selection of physically unrealistic EMs.

In this paper, we develop an improved algorithm for FORC-PCA that addresses these issues. We present a practical implementation that allows the FORC distribution and the FORCs themselves to be reconstructed simultaneously, and describe objective criteria that can be used to guide the most appropriate EM choice to enable quantitative unmixing of FORC diagrams. These improvements to the FORC-PCA method are implemented and integrated into a new version of the FORCem package within FORCinel (Harrison & Feinberg, 2008; Lascu et al., 2015), as described in supporting information.

2. Materials and Methods

Three synthetic binary mixtures that contain known proportions of SD, V, and MD magnetite were studied using FORC-PCA. Binary mixtures of SD-V and SD-MD particles were kindly provided by Bruce Moskowitz of the Institute for Rock Magnetism. These samples have been used in several previous studies of magnetic unmixing (Carter-Stiglitz et al., 2001; Dunlop & Carter-Stiglitz, 2006; Lascu et al., 2010). The SD EM is a freeze-dried sample of a cultivated strain of the MV1 magnetotactic bacterium. The magnetosomes have a well-constrained grain-size distribution, with particle sizes of $35 \times 35 \times 53$ nm aligned in chains of 10–20 crystals (Moskowitz et al., 1993). Both the V and MD EMs are synthetic magnetites produced by Wright Industries, with typical grain-size distributions of 1–3 and 8–40 μm , respectively (Carvallo & Muxworthy, 2006). The SD-V and SD-MD mixtures were produced by first dispersing the coarser EM in CaF_2 to 0.1% by weight and then adding MV1 to obtain the desired mass proportions. The V-MD mixture was created by weighing the mass of EMs, and dispersing them to a 1% concentration in a fine-grained sucrose matrix. Samples were mixed gently, placed into gelatin capsules, and packed with quartz wool or Kimwipe tissues to prevent vibration of the sample during measurement. The mixing proportions of all samples are listed in Table 1. Bulk hysteresis parameters (newly measured for this study) for all samples are listed in Table 2.

Measurements were made at the University of Cambridge on a Lakeshore PMC MicroMag vibrating sample magnetometer. For each sample, 174 FORCs were acquired in 1.5 mT field increments with 200 ms averaging time. The FORC data were imported into FORCinel (Harrison & Feinberg, 2008) and processed using the VARIFORC smoothing algorithm (Egli, 2013), resampled on a 2 mT grid, and subjected to PCA analysis following the protocol described by Lascu et al. (2015). EMs were selected from known pure samples to constrain the mixing space. In each case, the finest magnetic component was chosen as EM1. The synthetic binary mixtures were then unmixed using PCA and the mixing proportions were calculated.

3. Results

Representative FORC diagrams for each set of studied binary mixtures are shown in Figures 1–3. The MD EM (Figures 1a and 3c) has a typical MD FORC diagram dominated by a low-coercivity, vertically spread signal and a weak, high-coercivity, horizontally spread tail, likely related to strong pinning of domain walls by stress fields on surfaces and at internal defects/dislocations (Lindquist et al., 2015; Pike et al., 2001a). The SD EM (Figures 1c and 2c) has a typical SD FORC diagram for noninteracting uniaxial SD particles, comprising

Table 1
Mass Fractions of End-Members in Measured Samples

Sample	SD	V	MD
<i>V-MD</i>			
wm_1		1.00	0.00
wm_2		0.85	0.15
wm_3		0.65	0.35
wm_4		0.64	0.36
wm_5		0.49	0.51
wm_6		0.69	0.31
wm_7		0.31	0.69
wm_8		0.34	0.66
wm_9		0.10	0.90
wm_10		0.00	1.00
wm_11		0.25	0.75
wm_12		0.42	0.58
<i>SD-V</i>			
w30_1	0.00	1.00	
w30_2	0.50	0.50	
w30_3	0.31	0.69	
w30_4	0.20	0.80	
w30_5	0.10	0.90	
w30_6	0.06	0.94	
w30_7	0.69	0.31	
w30_8	0.80	0.20	
w30_9	0.90	0.10	
w30_10	0.95	0.05	
<i>SD-MD</i>			
w14_1	0.00		1.00
w14_2	0.56		0.44
w14_3	0.33		0.67
w14_4	0.24		0.76
w14_5	0.12		0.88
w14_6	0.83		0.17
w14_7	0.92		0.08

an intense horizontal ridge and a corresponding weak negative signal located close to the negative B_u axis (Egli et al., 2010; Muxworthy et al., 2004; Newell, 2005). The coercivity distribution for the cultured MV1 bacteria is particularly narrow. Some vertical spreading of the horizontal ridge is evident, which indicates either the presence of magnetic interactions among the magnetosome chains, or a small degree of chain collapse (Egli & Winklhofer, 2014; Harrison & Lascu, 2014; Li et al., 2012). A slight vertical offset of the horizontal ridge is likely a viscous magnetization effect caused by the time asymmetry of the FORC measurement protocol (Egli, 2013). The V EM (Figures 2a and 3a) consists of an intense, closed-contour peak with broad vertical and horizontal spreading, and three weaker, less prominent lobes. Although such FORC signatures can be created by strongly interacting SD clusters (e.g., Carvallo et al., 2005), this explanation can be ruled out here because the known grain size of the sample (1–3 μm) far exceeds the upper SD threshold size. Instead, the broad central peak and three lobes are interpreted as MV and SV processes, respectively, dominated by intraparticle, rather than interparticle, interactions. A weak negative signal close to the negative B_u axis is visible in Figure 3a. For V-MD mixtures, the maximum intensity of the FORC signal in each EM is comparable, so that both signals are clearly evident in a ~50:50 mixture (Figure 3b). The intense positive signal associated with the SD EM, however, dominates the FORC signal of the SD-MD and SD-V mixtures (Figures 1b and 2b), so that only when >80% of the mixture is constituted by the MD or V EMs does their presence become obvious in the FORC diagram.

Results of FORC-PCA analysis using the method of Lascu et al. (2015) are shown in Figure 4. There is a systematic nonlinear deviation in all three mixtures between the FORC-PCA calculated (EM1) and actual weight fractions (EM1*) of EMs used to prepare the samples. With EM1 defined to be the finer-grained EM, all three binary mixtures have a concave down relationship between the calculated versus

actual mixing proportions. The nonlinearity is most pronounced for the SD-MD binary mixture, and is least pronounced for the SD-V binary mixture.

4. Origin of the Unmixing Discrepancy

The difference between mixing proportions derived by FORC-PCA and the known mass proportions of EMs in the synthetic mixtures (Figure 4) can be explained by the fact that the SD, V, and MD states have different ratios of irreversible to reversible magnetization. The FORC distribution, ρ , is defined as:

$$\rho = -\frac{1}{2} \frac{\partial^2 M}{\partial B_a \partial B_b}, \quad (1)$$

where M is the magnetization, B_a is the reversal field, and B_b is the measurement field. Prior to FORC-PCA analysis, each FORC diagram is normalized by its integral:

$$\iint \rho dB_a dB_b = M_s - M_{\text{rev}} = M_{\text{irr}}, \quad (2)$$

where M_s is the saturation magnetization, M_{rev} is the reversible component, and M_{irr} is the irreversible component (Pike, 2003). FORC-PCA describes each normalized FORC diagram as the linear sum of normalized EMs, so that the mixing proportions are defined as (e.g., for a binary mixture):

$$\text{EM1} = \frac{m_1 M_{s1} f_1}{M_{\text{irr}}} \quad \text{and} \quad (3)$$

Table 2
Summary of Hysteresis Properties for Measured Samples

Sample	H_c (mT)	H_{cr} (mT)	H_{cr}/H_c	M_r/M_s
<i>V-MD</i>				
wm_1	31.35	52.56	1.68	0.29
wm_2	28.61	52.23	1.83	0.26
wm_3	23.11	79.32	3.43	0.20
wm_4	21.05	49.43	2.35	0.19
wm_5	18.25	48.59	2.66	0.16
wm_6	22.89	48.59	2.12	0.20
wm_7	13.70	46.04	3.36	0.12
wm_8	15.18	46.82	3.08	0.13
wm_9	2.59	34.53	13.36	0.03
wm_10	4.39	23.70	5.40	0.04
wm_11	11.11	42.61	3.83	0.09
wm_12	16.35	47.93	2.93	0.14
<i>SD-V</i>				
w30_1	24.20	45.26	1.87	0.02
w30_2	41.17	52.96	1.29	0.35
w30_3	35.85	52.79	1.47	0.29
w30_4	31.75	52.11	1.64	0.26
w30_5	27.55	50.56	1.84	0.23
w30_6	26.63	50.01	1.88	0.23
w30_7	41.34	49.42	1.20	0.40
w30_8	41.62	48.71	1.17	0.43
w30_9	41.78	48.63	1.16	0.47
w30_10	41.88	47.61	1.14	0.48
<i>SD-MD</i>				
w14_1	5.47	26.11	4.77	0.04
w14_2	34.24	49.43	1.44	0.27
w14_3	21.26	48.75	2.29	0.16
w14_4	16.52	47.85	2.90	0.13
w14_5	10.57	44.81	4.24	0.09
w14_6	41.45	49.35	1.19	0.40
w14_7	42.80	49.49	1.16	0.45

$$EM2 = 1 - EM1 = \frac{m_2 M_{s2} f_2}{M_{irr}}, \quad (4)$$

where m_1 and m_2 are the mass of each EM, M_{s1} and M_{s2} are the mass-normalized saturation magnetization of each EM, and f_1 and f_2 are the ratio of the irreversible magnetization to saturation magnetization for each EM. The mass proportions of the EMs in the mixture are given by:

$$EM1^* = \frac{m_1}{m_1 + m_2}. \quad (5)$$

Rearranging equations (3) and (4) and substituting in (5), we obtain:

$$EM1^* = \frac{EM1}{EM1 + f(1 - EM1)}, \quad (6)$$

where

$$f = \frac{M_{s1} f_1}{M_{s2} f_2}. \quad (7)$$

The f factor expresses how different the EMs are in terms of their irreversible/reversible magnetization contributions. A value of $f = 1$ corresponds to ideal behavior ($EM^* = EM1$), and is obtained only when the EMs contain identical minerals ($M_{s1} = M_{s2}$) with equal ratios of irreversible to saturation magnetization ($f_1 = f_2$). Least squares fits to plots of $EM1$ versus $EM1^*$ are shown as solid lines in Figure 4, yielding f values of 2.72, 1.52, and 2.69 for the SD-MD, SD-V, and V-MD mixtures, respectively. All EMs contain magnetite; therefore, the different f factors indicate that the irreversible contribution to the magnetization of each domain state is different, with $SD > V > MD$. Although, in principle, equation (6) allows the FORC-PCA proportions to be corrected, prior knowledge of the f factor is required. This is not a practical solution when the properties of the EMs are unknown.

5. An Improved FORC-PCA Algorithm

The nonlinear unmixing discrepancy documented above can be corrected by applying PCA to the FORC magnetization surface (which contains both reversible and irreversible contributions), rather than to the FORC distribution (which contains only irreversible contributions); the FORC magnetization surface has been shown previously to mix linearly (Muxworthy et al., 2005). This approach, however, poses a challenge to interactive exploration of the unmixing space that is necessary to identify suitable EMs: as each point in the mixing space is explored, it becomes necessary to estimate ρ over the reconstructed magnetization surface to obtain the corresponding FORC diagram. Here we overcome this problem by applying PCA to the set of six polynomial coefficients that are used to fit the magnetization surface during smoothing of the input FORC diagrams (Pike et al., 1999). In this way, the reconstructed set of coefficients at any given point in the unmixing space can be used to calculate both the magnetization surface and its derivatives simultaneously.

Our procedure is described as follows. Raw FORC data for a set of samples to be analyzed are imported into FORCinel. A linear high-field slope correction is applied, and a record is kept of the mass normalized M_s value for each sample, for future reference. Here the slope correction was performed by fitting a straight line to the high-field portion of the FORCs. In cases where the FORCs have not been measured to sufficiently high fields to fully saturate the ferrimagnetic component, it may be desirable to perform the correction using a separately determined value of the high-field susceptibility. The FORCs are normalized to $M_s = 1$, the lower-branch subtracted (optionally), and processed using the VARIFORC variable smoothing algorithm (Egli, 2013). For consistency with the published code (see supporting information) we use the VARIFORC

Table 3
Summary of Hysteresis Properties for Extracted EMs

	H_c (mT)	H_{cr}	H_{cr}/H_c	M_r/M_s
<i>V-MD</i>				
EM1	33.0	52.6	1.6	0.38
EM2	4.6	24.5	5.3	0.044
V (obs)	31.0	52.9	1.7	0.37
MD (obs)	4.5	24.4	5.5	0.045
<i>SD-V</i>				
EM1	27.0	49.0	1.8	0.34
EM2	42.0	48.0	1.1	0.54
EM3	39.0	45.0	1.2	0.54
SD (95%)	41.0	48.0	1.2	0.52
V (obs)	24	48.5	2.0	0.34
<i>SD-MD</i>				
EM1	6.0	26.8	4.5	0.07
EM2	41.0	47.5	1.2	0.53
EM3	37.5	43.5	1.2	0.55
SD (92%)	39.7	47.5	1.2	0.49
MD (obs)	5.2	26.9	5.1	0.07

coordinate scheme (B_c, B_u) rather than the measurement coordinate scheme (B_a, B_b) in the following. For each output point in a processed FORC diagram, a weighted second-order polynomial fit is performed to the local magnetization surface over a rectangular area defined by the horizontal and vertical smoothing factors (Egli, 2013):

$$M(B_c, B_u) = a_0 + a_1 B_c + a_2 B_u + a_3 B_c^2 + a_4 B_c B_u + a_5 B_u^2 \quad (8)$$

The FORC distribution (equation (1)) is then given by:

$$\rho = \frac{a_3 - a_5}{4} \quad (9)$$

In order to analyze sets of FORC diagrams that may have been acquired using different measurement protocols, each polynomial coefficient in equation (8) is interpolated bilinearly onto a rectangular grid, capturing a specified region of interest. For a rectangular grid containing N points, there will be $6N$ observations for each FORC diagram, corresponding to the six bilinearly interpolated polynomial coefficients for each point. The FORC-PCA method of Lascau et al. (2015) is then applied, simply replacing the N values of the FORC distribution with the $6N$ polynomial coefficients for each sample. Once

the number of significant PCs has been chosen ($n \leq 3$, corresponding to a maximum of four EMs), low-rank approximations of both the magnetization surface and the FORC distribution can be reconstructed for any chosen location within the resulting unmixing space (score plot). Exploring the unmixing space to identify potential EMs can now be performed interactively, guided by both the reconstructed magnetization and corresponding FORC diagram.

A complication occurs when the option to subtract the lower branch from the normalized FORCs prior to smoothing is chosen. Lower-branch subtraction was introduced by Egli (2013) to improve smoothing performance in the vicinity of the $B_b = 0$ axis (an axis extending from the origin at a -45° angle in VARIFORC coordinate space). Lower-branch subtraction reduces significantly the appearance of smoothing artifacts along this axis when using variable smoothing protocols because it removes sigmoidal magnetization contributions that are poorly described by a second-order polynomial. When smoothing is performed after

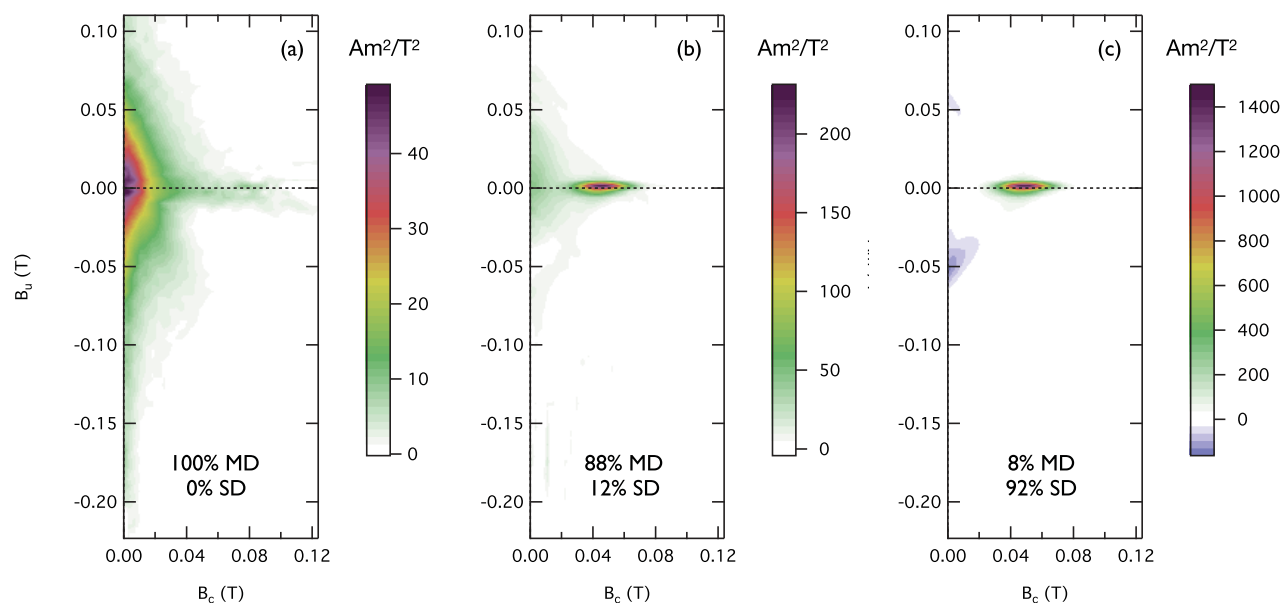


Figure 1. Experimental FORC diagrams for SD-MD mixtures. Smoothing performed using FORCinel with VARIFORC parameters $S_{c0} = 7$, $S_{c1} = 7$, $S_{b0} = 5$, $S_{b1} = 7$, $\lambda_c = 0.1$, and $\lambda_b = 0.1$. Mixing proportions are (a) 100% MD, 0% SD, (b) 88% MD, 12% SD, and (c) 8% MD, 92% SD.

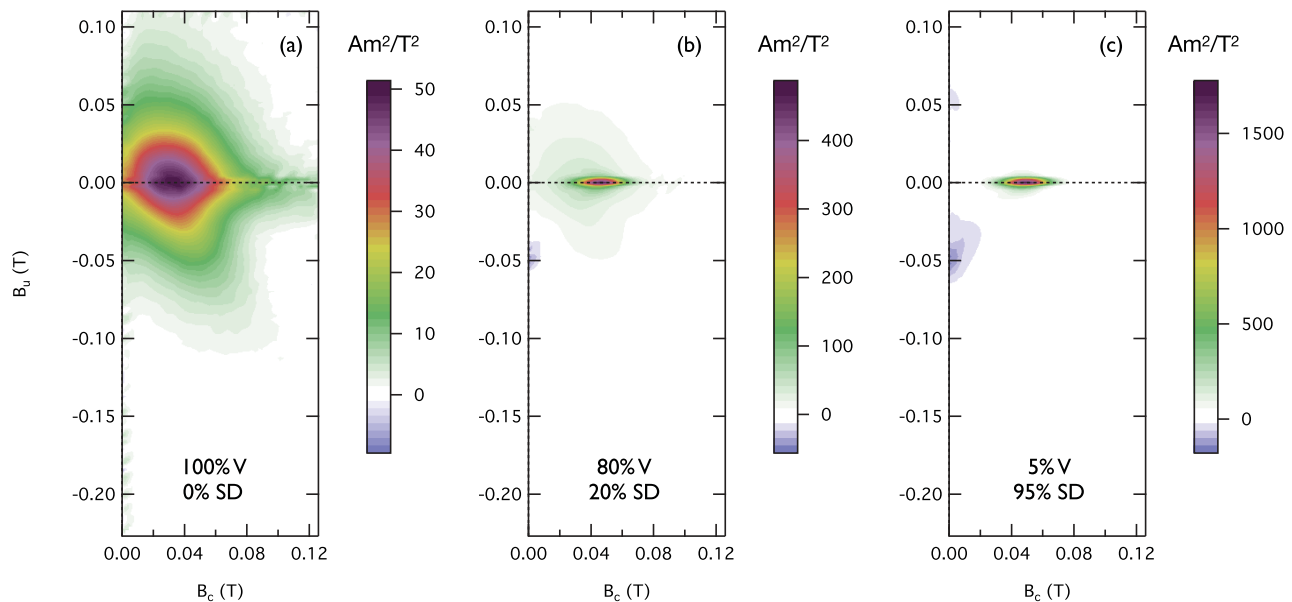


Figure 2. Experimental FORC diagrams for SD-V mixtures. Smoothing performed using FORCinel with VARIFORC parameters $S_{c0} = 7$, $S_{c1} = 12$, $S_{b0} = 5$, $S_{b1} = 12$, $\lambda_c = 0$, and $\lambda_b = 0$. Mixing proportions are (a) 100% V, 0% SD, (b) 80% V, 20% SD, and (c) 5% V, 95% SD.

lower-branch subtraction, the set of polynomial coefficients in equation (8) describes the subtracted magnetization surface rather than the desired full magnetization surface. In order to reconstruct the full magnetization surface, a second smoothing step is performed on a synthetic 2-D magnetization surface created using just the lower-branch signal. This lower-branch surface is fitted using equation (8), but with the strict constraint that $a_3 = a_5$, thereby ensuring that the FORC distribution (and its associated artifacts) associated with the lower-branch surface is zero (equation (9)). Polynomial coefficients resulting from the fit to the lower-branch surface are then added to those resulting from the fit to the lower-branch subtracted

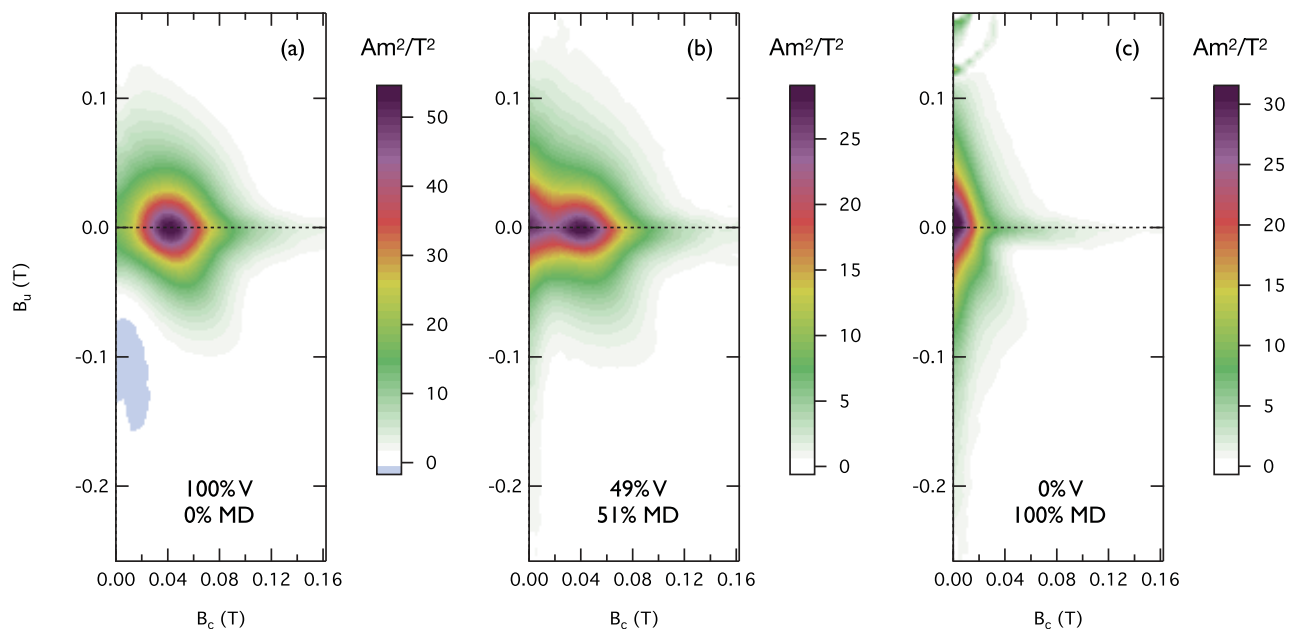


Figure 3. Experimental FORC diagrams for V-MD mixtures. Smoothing performed using FORCinel with VARIFORC parameters $S_{c0} = 7$, $S_{c1} = 7$, $S_{b0} = 5$, $S_{b1} = 7$, $\lambda_c = 0.1$, and $\lambda_b = 0.1$. Mixing proportions are (a) 100% V, 0% MD, (b) 49% V, 51% MD, and (c) 0% V, 100% MD.

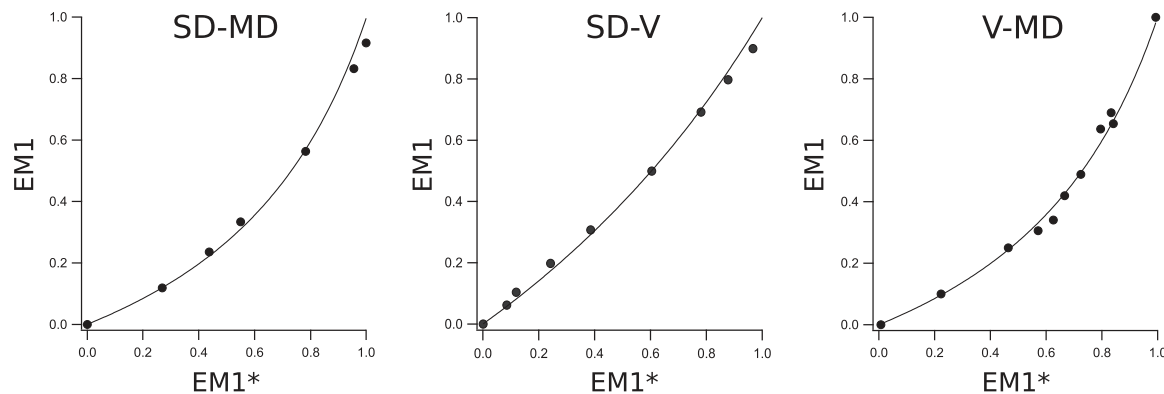


Figure 4. Comparison of mixing proportions derived from FORC-PCA (EM) using the method of Lascau et al. (2015) with known mass proportions of end-members in synthetic mixtures (EM*) of (a) SD-MD, (b) SD-V, and (c) V-MD magnetite particles, respectively. Solid lines are fits to the data using equation (6), which yield $f = 2.72, 1.52, \text{ and } 2.69$, respectively.

magnetization surface, which are then used as input to the FORC-PCA. This double-smoothing procedure allows the full magnetization surface to be reconstructed from the chosen PC combination, while retaining an artifact-free representation of the reconstructed FORC diagram.

Heslop and Roberts (2012a) demonstrated that, because of the corrupting effects of measurement noise, it is necessary to calculate statistical significance levels to identify the parts of an FORC distribution, where ρ is significantly above the signal-to-noise ratio. Use of PCA to provide a low-rank approximation of a collection of measured FORC diagrams is also an effective approach to reduce the influence of noise in representing a mixing system (Heslop, 2015). Therefore, while PCA will not eliminate noise completely, its effect on the representation of the mixing system and on the identified EMs is reduced substantially compared to individual FORC diagrams.

Results of the new algorithm applied to the synthetic binary mixtures are shown in Figures 5–7. The V-MD mixture (Figure 5) is well described as a binary mixture, with 99% of the variance in the data set explained by PC1. Pure EMs are included within the data set, which leads to no ambiguity in the choice of EM1 (V) and EM2 (MD) (Figures 5a and 5b). The SD-MD mixture (Figure 6) can be approximated as a binary mixture, with 95% of the variance being explained by the first principal component (PC1). However, a small but significant second principal component (PC2) is needed to bring the variance explained to $>99\%$ (Figure 6g). Without including PC2, it is not possible to isolate completely a pure MD EM. This effect is caused by subtle coercivity differences of the MV1 bacteria from sample to sample, which only become apparent because of the intense and narrow nature of their FORC distribution. Possible explanations for the coercivity difference between samples include differences in oxidation state that resulted from sample storage in air for over 10 years, or different degrees of bacterial chain collapse. By including PC2, small coercivity differences can be taken into account, enabling a pure MD EM to be identified (EM1, Figure 6a), along with two SD EMs (EM2 and EM3) that differ only in their average coercivity (Figures 6b and 6c, and Table 3). Hence, PC1 describes the binary mixing between SD and MD EMs, and PC2 accounts for the varying coercivity of the SD MV1 component. A similar approach was taken to describe the SD-V mixture (Figure 7), although the coercivity variation of the MV1 samples is less pronounced (99% of the variance is explained by PC1 alone). In all three cases, the mixing proportions derived from FORC-PCA agree well with the known mass fractions. The 2σ differences between calculated and observed proportions are 2%, 5%, and 6% for the SD-MV, SD-V, and MD-V binary mixtures, respectively. These observations provide an empirical estimate of the error in the unmixing proportions that is likely to be achieved using FORC-PCA in optimal cases (i.e., where the mixing space is well sampled by the data set).

6. Feasibility Metrics

An inherent part of the FORC-PCA method is the supervised exploration of the unmixing space in order to identify appropriate EMs (Lascau et al., 2015). This process is only unambiguous when the sample set includes examples of each EM that is being solved for (as is approximately the case for the binary mixtures

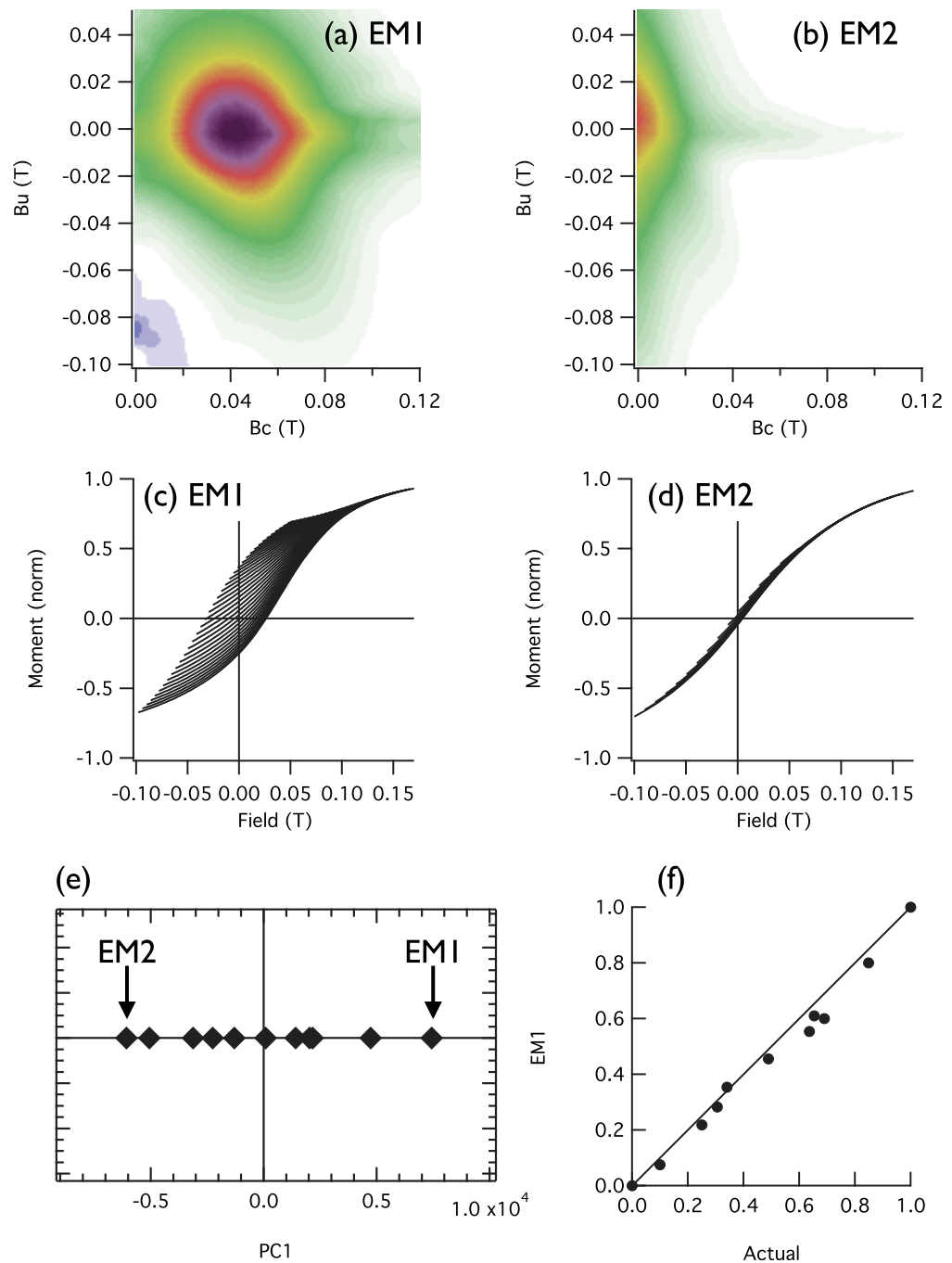


Figure 5. FORC-PCA analysis of V-MD mixtures using the new unmixing algorithm. (a and b) Reconstructed FORC diagrams for EM1 (V) and EM2 (MD). (c and d) Reconstructed FORCs for EM1 and EM2. (e) PC score plot for a binary unmixing space between EM1 and EM2 (indicated by arrows). Diamonds illustrate the scores of individual samples. (f) Comparison of mixing proportions extracted using the new algorithm with the known mass proportions of end-members in the synthetic mixture. The solid line indicates a one-to-one relationship.

studied here). When the sampling of the unmixing space is incomplete, however, the method relies heavily on the expertise of the user to identify (a) EMs that enclose the entire set of sample scores (with the exception of outliers identified by residual analysis), (b) pure EMs (i.e., that do not contain any residual contributions from the other EMs), and (c) EMs that are physically realistic (i.e., the reconstructed FORC diagram for each EM corresponds to an achievable FORC geometry based on the knowledge of the magnetic

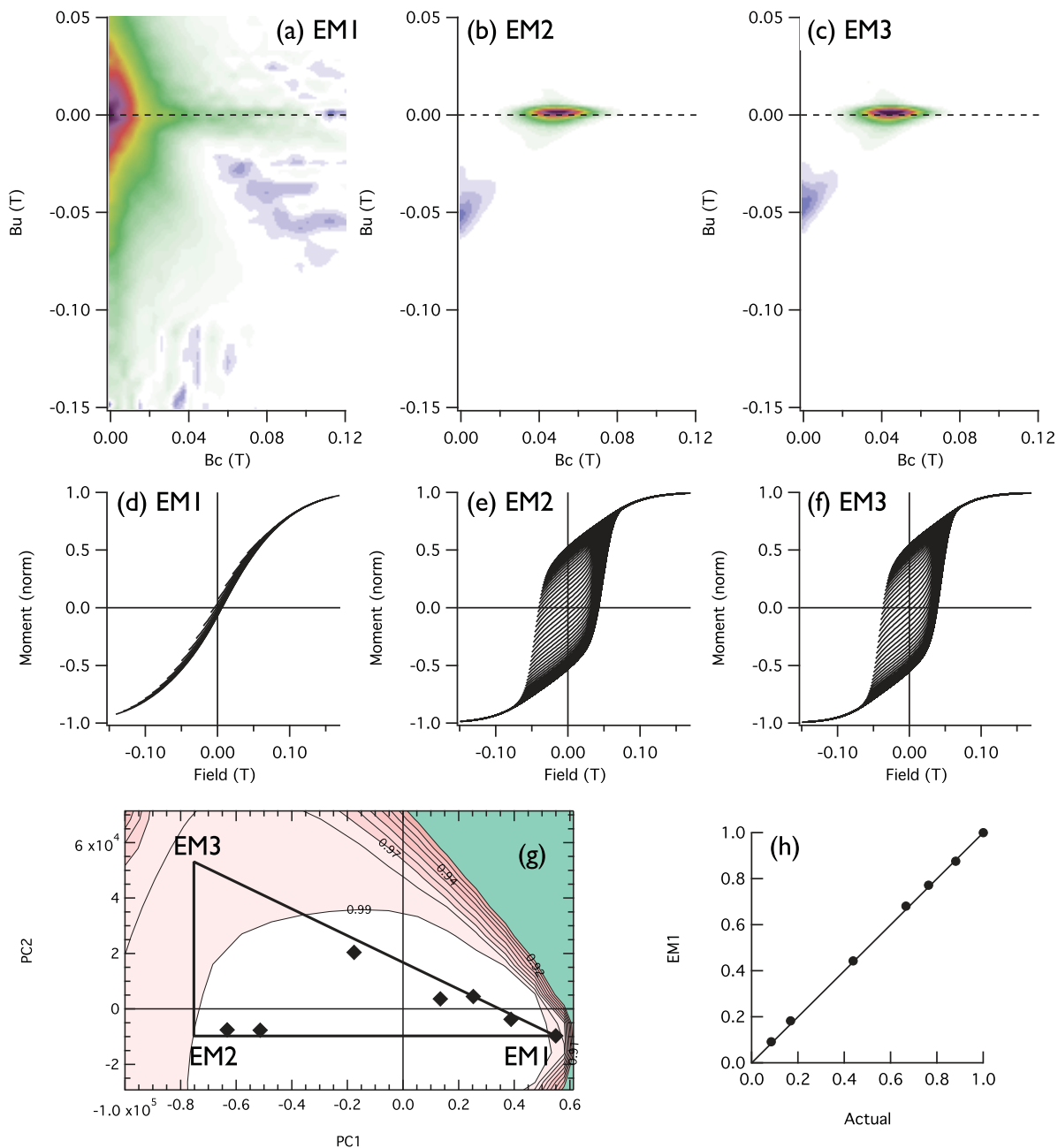


Figure 6. FORC-PCA analysis of MD-SD mixtures using the new algorithm. (a–c) Reconstructed FORC diagrams for EM1 (MD), EM2 (SD high coercivity), and SD (low coercivity), respectively. (d–f) Reconstructed FORCs for EM1, EM2, and EM3, respectively. (g) PC score plot for a ternary unmixing space between EM1, EM2, and EM3 (black triangle). Diamonds illustrate the scores of individual samples. Contour lines represent the combined feasibility metric, *m*, for the saturation, monotonicity, and crossing metrics. (h) Comparison of mixing proportions extracted using the new algorithm with the known mass proportions of end-members in the synthetic mixture. The solid line represents a one-to-one relationship.

mineralogy and the responses that can be modeled physically) (Harrison & Lascau, 2014). With access to only the reconstructed FORC diagram, identification of physically unrealistic regions of the unmixing space relies on subjective criteria. The availability of reconstructed FORCs, however, provides objective information from which criteria can be defined to assess the physical feasibility of the corresponding FORC diagram. Following the approach of Heslop and Roberts (2012b), three criteria that can be applied to assess the feasibility of reconstructed FORCs are: (a) saturation (i.e., no FORC should exceed the normalized value of $M_s = 1$), (b)

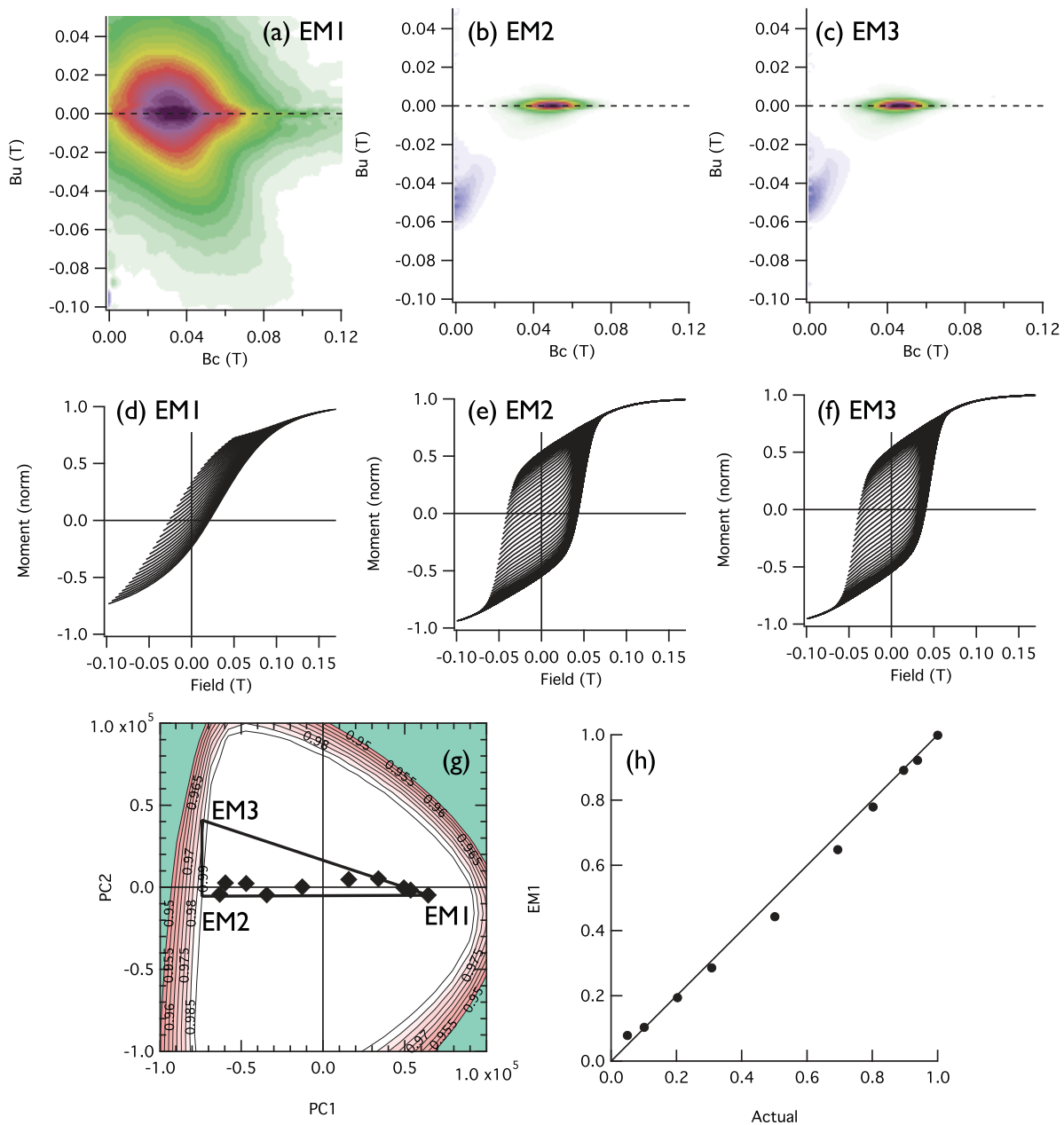


Figure 7. FORC-PCA analysis of V-SD mixtures using the new algorithm. (a–c) Reconstructed FORC diagrams for EM1 (V), EM2 (SD high coercivity), and SD (low coercivity), respectively. (d–f) Reconstructed FORCs for EM1, EM2, and EM3, respectively. (g) PC score plot for a ternary unmixing space between EM1, EM2, and EM3 (black triangle). Diamonds illustrate the scores of individual samples. Contour lines represent the combined feasibility metric for the saturation, monotonicity, and crossing metrics. (h) Comparison of mixing proportions extracted using the new algorithm with the known mass proportions of end-members in the synthetic mixture. The solid line represents a one-to-one relationship.

monotonicity (i.e., the first derivative of a FORC with respect to the measurement field should remain non-negative), and (c) crossing (i.e., the first derivative of the magnetization surface with respect to the reversal field should remain positive, meaning that FORCs do not intersect each other). Each of these metrics can be used on their own, or in combination, to define the region of unmixing space that is physically realistic. The EMs should be contained entirely within that region.

We define three metrics for each of the feasibility criteria, which vary from 0 (completely unsatisfied) to 1 (completely satisfied):

$$m_{\text{saturation}} = \frac{\sum |M_A|}{\sum |M|}, \quad (10)$$

where M_A is the subset of the magnetization, M , that satisfies the condition $|M| \leq 1$;

$$m_{\text{monotonicity}} = \frac{\sum \left(\frac{dM}{dB_a}\right)_A}{\sum \left|\frac{dM}{dB_a}\right|}, \quad (11)$$

where $\left(\frac{dM}{dB_a}\right)_A$ is the subset of $\frac{dM}{dB_a}$ that satisfies the condition $\frac{dM}{dB_a} \geq 0$; and

$$m_{\text{crossing}} = \frac{\sum \left(\frac{dM}{dB_b}\right)_A}{\sum \left|\frac{dM}{dB_b}\right|}, \quad (12)$$

where $\left(\frac{dM}{dB_b}\right)_A$ is the subset of $\frac{dM}{dB_b}$ that satisfies the condition $\frac{dM}{dB_b} \geq 0$.

The metrics can be combined into a single feasibility metric, m , by multiplying them together in any combination. By calculating m over a grid of points, contours of feasibility can be used to indicate the region of unmixing space, where the criteria are satisfied fully ($m = 1$). In practice, some allowance is needed for the fact that we are dealing with a low-rank approximation to the data, that some nonmonotonicity may be genuinely present (e.g., for SP grains), and that experimental noise can cause FORCs to cross as saturation is approached. This means that m values slightly less than 1 should be allowable. Here we take $m > 0.99$ as a reasonable (although arbitrary) guideline of acceptability (Figures 6g and 7g). Given the essentially binary nature of the mixtures, the placement of EM3 slightly outside the $m = 0.99$ contour in Figures 6g and 7g has been done to maintain EM2 and EM3 at a constant value of PC1 away from EM1, while ensuring that all data points are contained within the mixing triangle.

A fourth metric, which should be used independently of the other three, describes the amount of negative signal in the processed FORC diagram. Given that negative regions are an intrinsic feature of many FORC diagrams, this metric is less stringent than the others (values significantly < 1 are acceptable). However, there are specific domain states that do not have intrinsically negative regions, or have only weakly negative regions, so evaluating this metric can be helpful to define the location of specific EMs. For example, inappropriate appearance of strong negative signals can be caused by over subtraction of other EMs, which provides a good indication that EM selection has strayed too far from the data. The positivity metric is defined as:

$$m_{\text{positivity}} = \frac{\sum |\rho_A|}{\sum |\rho|}, \quad (13)$$

where ρ_A is the subset of the FORC distribution, ρ , that satisfies the conditions $\rho \geq 0$. Steep drops in $m_{\text{positivity}}$ may indicate that over subtraction of other EMs is occurring.

7. Example

To illustrate the new FORC-PCA algorithm applied to natural mixtures of different domain states, we analyzed a suite of greigite-bearing clays from Florindo et al. (2007), which were deposited between 800 and 600 ka in the Tiber River coastal alluvial plain around Rome. A total of 17 FORCs were measured, 14 of which contain magnetostatically interacting SD greigite mixed with varying amounts of an SP/SD greigite. The other three samples contain the SP/SD signal only. The latter samples were significantly less magnetic than the former, and have noisy processed FORC diagrams. FORC data from these three samples were averaged to produce a single representative example of the pure SP/SD component. This averaged FORC and the other 14 FORCs were then analyzed using FORC-PCA (Figure 8). Only two PCs are needed to explain over 90% of the variance in the data set, with a third PC bringing the variance explained to 98%. For illustrative purposes, we use a two-PC model constructed from PC1 and PC3, which provides the most convenient projection of the key mixing trends. Three EMs are identified. Key features of EM1 (Figure 8a) are a negative region close to the negative B_u axis (1), a second negative region that is elongated and steeply angled down and to the right (2), and a kidney-shaped positive peak that is strongly offset in the negative B_u direction and extends only slightly above the $B_u = 0$ axis (3). All three of these features are diagnostic of relatively

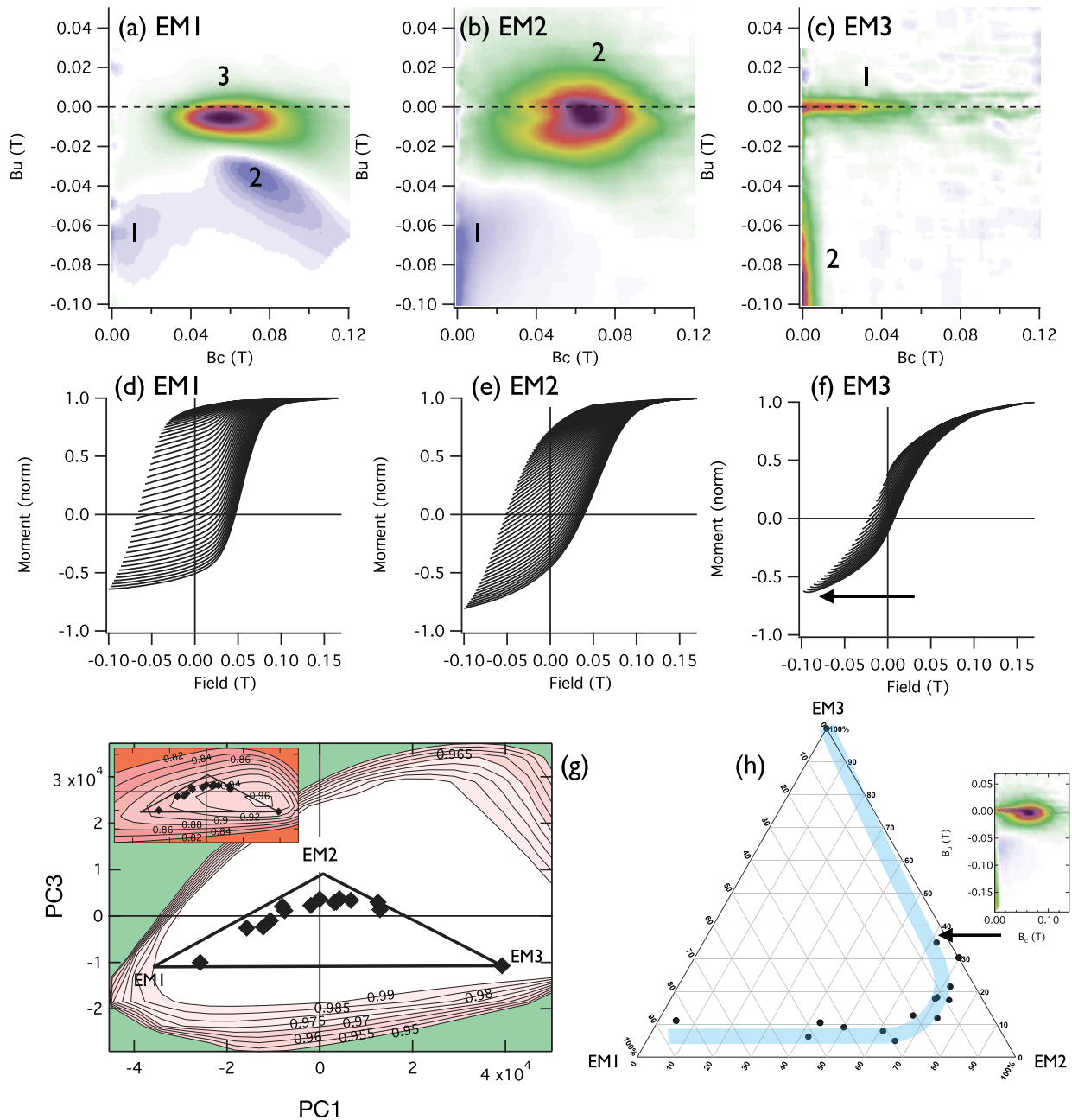


Figure 8. FORC-PCA analysis of greigite-bearing clay samples from the Tiber River, Rome (Florindo et al., 2007). (a–c) Reconstructed FORC diagrams for EM1 (moderately interacting SD greigite), EM2 (strongly interacting SD greigite) and EM3 (SP/SD greigite), respectively. (d–f) Reconstructed FORCs for EM1, EM2, and EM3. The arrow in Figure 8f indicates the downward-inflected response at the start of each FORC. Although this phenomenon is associated partially here with viscous SP behavior (Pike et al., 2001b), it is also likely to be partially an instrumental artifact in this case. (g) PC score plot for a ternary unmixing space between EM1, EM2, and EM3 (black triangle). Diamonds illustrate the scores of individual samples. Contour lines represent the combined feasibility metric for the saturation, monotonicity, and crossing metrics. The inset is an illustration of contours for the positivity metric. (h) Ternary diagram for the extracted proportions of EM1, EM2, and EM3. The blue line illustrates the two dominant mixing trends (EM3–EM2 and EM2–EM1). An example experimental FORC diagram for a mixture of strongly interacting and ~35% viscous SP/SD greigite is indicated by the arrow.

weakly interacting SD greigite grains (Roberts et al., 2011) with cubic magnetocrystalline anisotropy (Harrison & Lascu, 2014). Key features of EM2 (Figure 8b) are a negative region close to the negative B_u axis (1) and a rounded positive peak that is offset in the negative B_u direction and extends far above the $B_u = 0$ axis (2). Both features are diagnostic of strongly interacting SD greigite (Harrison & Lascu, 2014; Roberts

et al., 2011). Key features of EM3 (Figure 8c) are a low-coercivity ridge with maximum intensity at 0 mT (1) and an increasing positive signal extending along the negative B_u axis (2). Feature 1 is characteristic of non-interacting SD greigite particles with coercivities that have been reduced by thermal activation (Pike et al., 2001b; Rowan & Roberts, 2006). Feature 2 is likely due to viscous SP behavior, which leads to the negative initial slope of each FORC (arrow in Figure 8f; Pike et al., 2001b). However, given that the intensity of this feature continues to increase, even as reverse saturation is approached, it is also likely to be partially an instrumental artifact.

The choice of EMs in this case has been guided by the following principles. First, EM3 is fixed by inclusion of the pure SP/SD EM in the data set. This sample plots to the far right of the unmixing space (Figure 8g), close to but within the guideline boundary of physical feasibility. Moving left, away from EM3 in a direction parallel to the PC1 axis (which describes the largest mode of variability in the data set), yields a binary mixture of EM3 and a moderately interacting SD greigite EM (EM1). The most extreme left-hand data point lies close to the guideline boundary of physical feasibility. However, the FORC diagram for this data point contains a trace residual of EM3. In order to obtain a pure EM, one must move further to the left. The guideline boundary of physical feasibility places a limit on how far to the left one can go before the reconstructed FORCs for EM1 become physically unrealistic. We place EM1 at the $m = 0.99$ threshold, which yields a physically realistic pure EM with no residual trace of EM3. The placement of EM2 is more difficult because it lies well within the guideline region of physical feasibility. Here the positivity index (equation (13)) provides an additional guideline (inset to Figure 8g). A steep drop in $m_{\text{positivity}}$ is observed if EM2 is placed too far along the positive PC2 axis, which is caused by over subtraction of EM1 from the reconstructed FORC diagram. If EM2 is placed too far along the positive PC1 axis then not all the data are enclosed by the unmixing space. Combined, these two principles place important constraints on the location of EM2, and produce a reconstructed FORC diagram with a recognizable geometry and minimal residual traces of EM1 and EM3.

Having defined the unmixing space, the proportions of the three EMs can be determined (Figure 8h). Two distinct mixing trends can be identified in the data: a mixing between SP/SD and strongly interacting SD greigite, and one between weakly and strongly interacting SD greigite. The first mixing trend can be explained by grain growth of authigenic greigite from small, noninteracting particles below the SP threshold size to larger, stable SD particles in closely packed clusters within framboids with strong interactions (Rowan & Roberts, 2006). The second mixing trend can be explained as a weakening of the interactions between SD greigite particles, driven by a lowering of the packing fraction. A possible mechanism to explain this trend is the progressive replacement of strongly interacting greigite framboids by thermodynamically stable, paramagnetic pyrite. This process was recently identified by Ebert et al. (2018) using high-resolution magnetic force microscopy imaging. This interpretation is consistent with the lack of a mixing trend between EM1 (SP/SD) and EM3 (weakly interacting SD), which cannot be achieved in this pyrite replacement scenario without first going through the strongly interacting SD greigite EM.

8. Discussion

Unmixing the magnetic properties of rocks, sediments, and soils is a primary task in rock magnetism. Numerous methods exist to tackle this problem (e.g., Dunlop, 2002a, 2002b; Egli, 2004a, 2004b, 2004c; Franke et al. 2007; Heslop & Dillon, 2007; Kruiver et al., 2001; Lagroix & Guyodo, 2017; Lascu et al., 2010, 2015; Ludwig et al., 2013; Robertson & France, 1994) as well as an extensive toolbox of magnetic proxies that are designed to highlight specific magnetic mineralogy variations in environmental contexts (Evans & Heller, 2003; Liu et al., 2012). No single method is perfect for all cases, and usually a combination of methods is needed to unmix all magnetic components contained within a material. In particular, preparatory studies performed at high sampling resolution provide an efficient way to prescreen a data set, and to identify samples that are closest to potential EMs (e.g., EM3 in Figure 8). The FORC-PCA method is ideally suited to characterizing ferrimagnetic minerals, with an emphasis on discriminating populations of grains that differ in domain state, coercivity distribution, anisotropy, and interaction field (i.e., aspects to which FORC diagrams are particularly sensitive). Here we have resolved many of the outstanding issues associated with the original FORC-PCA method of Lascu et al. (2015), including solution of the linear mixing equation, the ability to identify SP EMs that are dominated by reversible magnetizations, and reducing ambiguities in defining the unmixing space. Excellent agreement between our calculated proportions for SD-MV and SD-V mixtures

contrasts starkly with attempts to unmix these samples using either linear or nonlinear mixing in a Day plot (Day et al., 1977; Dunlop & Carter-Stiglitz, 2006). Failure of the Day plot unmixing approach was explained by Dunlop and Carter-Stiglitz (2006) as due to the squareness of hysteresis loops for MV1 bacteria, which violates the linear assumption of the unmixing model (Dunlop, 2002a, 2002b). This illustrates one of the key advantages of PCA, which makes no prior assumptions about the shape of the EM signals (Heslop, 2015).

The need to use three EMs to describe binary SD-V and SD-MD mixtures highlights an important underlying assumption of the FORC-PCA method, namely that the properties of each EM are constant throughout a sample set, with only the mixing proportions varying from sample to sample. Whenever this assumption is not met, additional “fictive” EMs may be needed to define adequately the total variability within a data set. This is clearly the case for the MV1-bearing mixtures, where significant coercivity variations of the bacterial component exist from sample to sample. Given the narrow coercivity distribution of the MV1 bacteria, use of a third EM becomes necessary to isolate a pure V or MD EM. Most natural samples have broader coercivity distributions, however, and as long as intra-EM variability is low compared to inter-EM variability, “fictive” EMs are not typically necessary. The likelihood that “fictive” EMs will be needed to account for intra-EM variability increases as the size of the FORC data set increases. For large data sets, it may be necessary to perform a series of FORC-PCA analyses on subsets of the data. This approach allows commonalities between EMs extracted from different subsets to be identified, and the nature of intra-EM variability to be explored. In other cases (e.g., grain-size sorting of a detrital component), sample-to-sample variability is physically linked to a single EM with continuously variable properties, rather than to a mechanical mixture of EMs with fixed properties. In these cases, FORC-PCA generates two or more “fictive” EMs that recreate intersample variations, but do not correspond to fixed physical components of the system. Nevertheless, the mixing proportions of “fictive” EMs provide a useful coordinate system with which to quantify the extent of intersample variation, and may be used to identify variation trends and clusters of behavior.

The ability to unmix up to four EMs, each with their own distinct domain state, coercivity and interaction field distribution, takes us beyond the routine characterization that is commonly considered “good enough” for most paleomagnetic studies, and largely addresses the ambiguities (Roberts et al., 2018) involved in interpreting the widely used Day diagram (Day et al., 1977). Note that there is no limit on the number of EMs that can be mathematically defined, but visualization and interactive exploration of the unmixing space becomes impractical beyond four EMs. The new algorithm provides a full set of FORCs for each EM, which allows additional hysteresis properties to be derived. In some cases, this additional information can be used to check for consistency with the interpreted physical origin of each EM (e.g., if the FORC diagram of the EM suggests noninteracting, uniaxial SD behavior, then M_r/M_s values close to 0.5 and B_{cr}/B_c values close to 1 would be expected). Compared to a Day diagram, hysteresis ratios of extracted EMs acquire enhanced physical meaning because the effects of mixing have been deconvolved. The use of feasibility metrics reduces (but does not eliminate) the ambiguity involved in defining EMs when the unmixing space is sampled incompletely. This development should help to make the FORC-PCA method accessible to a wider audience. However, it should always be borne in mind that feasibility metrics are only a guideline—good choices, as ever, rely on the expertise and judgment of the user.

9. Conclusions

1. Our improved FORC-PCA algorithm addresses many of the outstanding issues with the initial method of Lascau et al. (2015), including solving the linear mixing problem and providing the ability to characterize SP EMs that are dominated by reversible magnetizations.
2. The new method enables both the reconstructed FORC magnetization surface and the corresponding FORC diagram of each EM to be identified.
3. Access to the reconstructed FORC magnetization surface enables objective criteria to be defined that guide the choice of physically realistic EMs. A mixture of robust criteria (e.g., saturation, monotonicity, and crossing) and more flexible criteria (e.g., positivity) can be used to help reduce the subjectivity of defining the unmixing space.
4. The method has been applied successfully to quantify synthetic binary mixtures with EMs with contrasting domain states, and to aid interpretation of diagenetic trends in greigite-bearing sedimentary environments.

- The improved FORC-PCA algorithm provides a powerful method to discriminate between populations of grains with different domain states, coercivity distribution, anisotropy type, and interaction field distribution. The increased value of the information that this analysis yields far outweighs the additional measurement time that is needed, providing a way to take routine rock magnetic characterization far beyond the ambiguities of the widely used Day diagram.

Acknowledgments

We thank Andrew Newell and Ramon Egli for their helpful and constructive reviews of the manuscript. This work was supported financially by the Australian Research Council through grant DP160100805 and by the European Research Council under the European Union's Seventh Framework Programme (FP/2007–2013)/ERC grant agreement 320750. Samples of SD-V and SD-MV mixtures were kindly provided by Bruce Moskowitz of the Institute for Rock Magnetism, University of Minnesota. All data used in this study are available for download as part of the online supporting information.

References

- Carter-Stiglitz, B., Moskowitz, B., & Jackson, M. (2001). Unmixing magnetic assemblages and the magnetic behavior of bimodal mixtures. *Journal of Geophysical Research*, *106*(B11), 26397. <https://doi.org/10.1029/2001JB000417>
- Carvalho, C., Dunlop, D., & Ozdemir, O. (2005). Experimental comparison of FORC and remanent Preisach diagrams. *Geophysical Journal International*, *162*, 747–754.
- Carvalho, C., & Muxworthy, A. (2006). Low-temperature first-order reversal curve (FORC) diagrams for synthetic and natural samples. *Geochemistry, Geophysics, Geosystems*, *7*, Q09003. <https://doi.org/10.1029/2006GC001299>
- Channell, J. E. T., Harrison, R. J., Lascu, I., McCave, I. N., Hibbert, F. D., & Austin, W. E. N. (2016). Magnetic record of deglaciation using FORC-PCA, sortable-silt grain size, and magnetic excursion at 26 ka, from the Rockall Trough (NE Atlantic). *Geochemistry, Geophysics, Geosystems*, *17*, 1823–1841. <https://doi.org/10.1002/2016GC006300>
- Day, R., Fuller, M., & Schmidt, V. A. (1977). Hysteresis properties of titanomagnetites: Grain-size and compositional dependence. *Physics of the Earth and Planetary Interiors*, *13*(4), 260–267.
- Donnelly, C., Guizar-Sicairos, M., Scagnoli, V., Gliga, S., Holler, M., Raabe, J., et al. (2017). Three-dimensional magnetization structures revealed with X-ray vector nanotomography. *Nature*, *547*(7663), 328–331. <https://doi.org/10.1038/nature23006>
- Dunlop, D. J. (2002a). Theory and application of the Day plot (M_{rs}/M_s versus H_{cr}/H_c) 1. Theoretical curves and tests using titanomagnetite data. *Journal of Geophysical Research*, *107*(B3), 2056. <https://doi.org/10.1029/2001JB000486>
- Dunlop, D. J. (2002b). Theory and application of the Day plot (M_{rs}/M_s versus H_{cr}/H_c) 2. Application to data for rocks, sediments, and soils. *Journal of Geophysical Research*, *107*(B3), 2057. <https://doi.org/10.1029/2001JB000487>
- Dunlop, D. J., & Carter-Stiglitz, B. (2006). Day plots of mixtures of superparamagnetic, single-domain, pseudosingle-domain, and multidomain magnetites. *Journal of Geophysical Research*, *111*, B12509. <https://doi.org/10.1029/2006JB004499>
- Ebert, Y., Shaar, R., Emmanuel, S., Nowaczyk, N., & Stein, M. (2018). Overwriting of sedimentary magnetism by bacterially mediated mineral alteration. *Geology*, *46*(4), 291–295. <https://doi.org/10.1130/G39706.1>
- Egli, R. (2004a). Characterization of individual rock magnetic components by analysis of remanence curves. 1. Unmixing natural sediments. *Studia Geophysica et Geodaetica*, *48*(2), 391–446. <https://doi.org/10.1023/B:SGEG.0000020839.45304.6d>
- Egli, R. (2004b). Characterization of individual rock magnetic components by analysis of remanence curves. *Physics and Chemistry of the Earth*, *29*(13–14), 851–867. <https://doi.org/10.1016/j.pce.2004.04.001>
- Egli, R. (2004c). Characterization of individual rock magnetic components by analysis of remanence curves. 3. Bacterial magnetite and natural processes in lakes. *Physics and Chemistry of the Earth*, *29*(13–14), 869–884. <https://doi.org/10.1016/j.pce.2004.03.010>
- Egli, R. (2006). Theoretical aspects of dipolar interactions and their appearance in first-order reversal curves of thermally activated single-domain particles. *Journal of Geophysical Research*, *111*, B12517. <https://doi.org/10.1029/2006JB004567>
- Egli, R. (2013). VARIFORC: An optimized protocol for calculating non-regular first-order reversal curve (FORC) diagrams. *Global and Planetary Change*, *110*, 302–320. <https://doi.org/10.1016/j.gloplacha.2013.08.003>
- Egli, R., Chen, A. P., Winklhofer, M., Kodama, K. P., & Horng, C.-S. (2010). Detection of noninteracting single domain particles using first-order reversal curve diagrams. *Geochemistry, Geophysics, Geosystems*, *11*, Q01Z11. <https://doi.org/10.1029/2009GC002916>
- Egli, R., & Winklhofer, M. (2014). Recent developments on processing and interpretation aspects of first-order reversal curves (FORC). *Proc. Kazan University*, *156*, 14–53.
- Evans, M. E., & Heller, F. (2003). *Environmental magnetism principles and applications of enviro-magnetics*. Amsterdam, Netherlands: Academic Press.
- Florindo, F., Karner, D., Marra, F., Renne, P. R., Roberts, A. P., & Weaver, R. (2007). Radiometric age constraints for Glacial Terminations IX and VII from aggradational sections of the Tiber River delta in Rome, Italy. *Earth and Planetary Science Letters*, *256*(1–2), 61–80. <https://doi.org/10.1016/j.epsl.2007.01.014>
- Franke, C., Frederichs, T., & Dekkers, M. J. (2007). Efficiency of heavy liquid separation to concentrate magnetic particles. *Geophysical Journal International*, *170*(3), 1053–1066. <https://doi.org/10.1111/j.1365-246X.2007.03489.x>
- Harrison, R. J., & Feinberg, J. M. (2008). FORCinel: An improved algorithm for calculating first-order reversal curve distributions using locally weighted regression smoothing. *Geochemistry, Geophysics, Geosystems*, *9*, Q05016. <https://doi.org/10.1029/2008GC001987>
- Harrison, R. J., & Lascu, I. (2014). FORCulator: A micromagnetic tool for simulating first-order reversal curve diagrams. *Geochemistry, Geophysics, Geosystems*, *15*, 4671–4691. <https://doi.org/10.1002/2014GC005582>
- Heslop, D. (2015). Numerical strategies for magnetic mineral unmixing. *Earth-Science Reviews*, *150*, 256–284. <https://doi.org/10.1016/j.earscirev.2015.07.007>
- Heslop, D., & Dillon, M. (2007). Unmixing magnetic remanence curves without a priori knowledge. *Geophysical Journal International*, *170*(2), 556–566. <https://doi.org/10.1111/j.1365-246X.2007.03432.x>
- Heslop, D., & Roberts, A. P. (2012a). Estimation of significance levels and confidence intervals for first-order reversal curve distributions. *Geochemistry Geophysics Geosystems*, *13*, Q12Z40. <https://doi.org/10.1029/2012GC004115>
- Heslop, D., & Roberts, A. P. (2012b). A method for unmixing magnetic hysteresis loops. *Journal of Geophysical Research*, *117*, B03103. <https://doi.org/10.1029/2011JB008859>
- Heslop, D., Roberts, A. P., & Chang, L. (2014). Characterizing magnetofossils from first-order reversal curve (FORC) central ridge signatures. *Geochemistry, Geophysics, Geosystems*, *15*, 2170–2179. <https://doi.org/10.1002/2014GC005291>
- Jolliffe, I. T. (2002). *Principal component analysis* (pp. 488). New York, NY: Springer-Verlag.
- Kruiver, P. P., Dekkers, M. J., & Heslop, D. (2001). Quantification of magnetic coercivity components by the analysis of acquisition curves of isothermal remanent magnetisation. *Earth and Planetary Science Letters*, *189*(3–4), 269–276. [https://doi.org/10.1016/S0012-821X\(01\)00367-3](https://doi.org/10.1016/S0012-821X(01)00367-3)
- Lagroix, F., & Guyodo, Y. (2017). A new tool for separating the magnetic mineralogy of complex mineral assemblages from low temperature magnetic behavior. *Frontiers in Earth Science*, *5*, 1–11. <https://doi.org/10.3389/feart.2017.00061>

- Lascu, I., Banerjee, S. K., & Berquó, T. S. (2010). Quantifying the concentration of ferrimagnetic particles in sediments using rock magnetic methods. *Geochemistry, Geophysics, Geosystems*, *11*, Q08Z19. <https://doi.org/10.1029/2010GC003182>
- Lascu, I., Harrison, R. J., Li, Y., Muraszko, J. R., Channell, J. E. T., Piotrowski, A. M., et al. (2015). Magnetic unmixing of first-order reversal curve diagrams using principal component analysis. *Geochemistry, Geophysics, Geosystems*, *16*, 2900–2915. <https://doi.org/10.1002/2015GC005909>
- Li, J., Wu, W., Liu, Q., & Pan, Y. (2012). Magnetic anisotropy, magnetostatic interactions and identification of magnetofossils. *Geochemistry, Geophysics, Geosystems*, *13*, Q10Z51. <https://doi.org/10.1029/2012GC004384>
- Lindquist, A. K., Feinberg, J. M., Harrison, R. J., Loudon, J. C., & Newell, A. J. (2015). Domain wall pinning and dislocations: Investigating magnetite deformed under conditions analogous to nature using transmission electron microscopy. *Journal of Geophysical Research: Solid Earth*, *120*, 1415–1430. <https://doi.org/10.1002/2014JB011335>
- Liu, Q., Roberts, A. P., Larrasoana, J. C., Banerjee, S. K., Guyodo, Y., Tauxe, L., et al. (2012). Environmental magnetism: Principles and applications. *Reviews of Geophysics*, *50*, RG4002. <https://doi.org/10.1029/2012RG000393>
- Ludwig, P., Egli, R., Bishop, S., Chernenko, V., Frederichs, T., Rugel, G., et al. (2013). Characterization of primary and secondary magnetite in marine sediment by combining chemical and magnetic unmixing techniques. *Global and Planetary Change*, *110*, 321–339. <https://doi.org/10.1016/j.gloplacha.2013.08.018>
- Maxbauer, D. P., Feinberg, J. M., Fox, D. L., & Nater, E. A. (2017). Response of pedogenic magnetite to changing vegetation in soils developed under uniform climate, topography, and parent material. *Scientific Reports*, *7*(1), 17575. <https://doi.org/10.1038/s41598-017-17722-2>
- Moskowitz, B., Frankel, R. B., & Bazylinski, D. A. (1993). Rock magnetic criteria for the detection of biogenic magnetite. *Earth and Planetary Science Letters*, *120*(3–4), 283–300.
- Muxworthy, A., Heslop, D., & Williams, W. (2004). Influence of magnetostatic interactions on first-order-reversal-curve (FORC) diagrams: A micromagnetic approach. *Geophysical Journal International*, *158*(3), 888–897. <https://doi.org/10.1111/j.1365-246X.2004.02358.x>
- Muxworthy, A. R., King, J., & Heslop, D. (2005). Assessing the ability of first-order reversal curve (FORC) diagrams to unravel complex magnetic signals. *Journal of Geophysical Research*, *110*, B01105. <https://doi.org/10.1029/2004JB003195>
- Newell, A. J. (2005). A high-precision model of first-order reversal curve (FORC) functions for single-domain ferromagnets with uniaxial anisotropy. *Geochemistry, Geophysics, Geosystems*, *6*, Q05010. <https://doi.org/10.1029/2004GC000877>
- Pike, C., Roberts, A., Dekkers, M., & Verosub, K. (2001). An investigation of multi-domain hysteresis mechanisms using FORC diagrams. *Physics of the Earth and Planetary Interiors*, *126*(1–2), 11–25.
- Pike, C. R. (2003). First-order reversal-curve diagrams and reversible magnetization. *Physical Review B*, *68*(10), 104424. <https://doi.org/10.1103/PhysRevB.68.104424>
- Pike, C. R., Roberts, A. P., & Verosub, K. L. (1999). Characterizing interactions in fine magnetic particle systems using first order reversal curves. *Journal of Applied Physics*, *85*(9), 6660–6667.
- Pike, C. R., Roberts, A. P., & Verosub, K. L. (2001). First-order reversal curve diagrams and thermal relaxation effects in magnetic particles. *Geophysical Journal International*, *145*(3), 721–730.
- Plaza-Morlote, M., Rey, D., Santos, J. F., Ribeiro, S., Heslop, D., Bernabeu, A., et al. (2017). Southernmost evidence of large European Ice Sheet-derived freshwater discharges during the Heinrich Stadials of the Last Glacial Period (Galician Interior Basin, Northwest Iberian Continental Margin). *Earth and Planetary Science Letters*, *457*, 213–226. <https://doi.org/10.1016/j.epsl.2016.10.020>
- Roberts, A., Chang, L., Rowan, C., Hornig, C., & Florindo, F. (2011). Magnetic properties of sedimentary greigite (Fe₃S₄): An update. *Reviews of Geophysics*, *49*, RG1002. <https://doi.org/10.1029/2010RG000336>
- Roberts, A. P., Almeida, T. P., Church, N. S., Harrison, R. J., Heslop, D., Li, Y., et al. (2017). Resolving the origin of pseudo-single domain magnetic behavior. *Journal of Geophysical Research: Solid Earth*, *122*, 9534–9558. <https://doi.org/10.1002/2017JB014860>
- Roberts, A. P., Heslop, D., Zhao, X., & Pike, C. R. (2014). Understanding fine magnetic particle systems through use of first-order reversal curve diagrams. *Reviews of Geophysics*, *52*, 557–602. <https://doi.org/10.1002/2014RG000462>
- Roberts, A. P., Pike, C. R., & Verosub, K. L. (2000). First order reversal curve diagrams: A new tool for characterising the magnetic properties of natural samples. *Journal of Geophysical Research*, *105*(B12), 28461–28475. <https://doi.org/10.1029/2000JB900326>
- Roberts, A. P., Tauxe, L., Heslop, D., Zhao, X., & Jiang, Z. (2018). A critical appraisal of the “Day” diagram. *Journal of Geophysical Research: Solid Earth*, *123*. <https://doi.org/10.1002/2017JB015247>
- Robertson, D. J., & France, D. E. (1994). Discrimination of remanence-carrying minerals in mixtures, using isothermal remanent magnetisation acquisition curves. *Physics of the Earth and Planetary Interiors*, *82*(3–4), 223–234. [https://doi.org/10.1016/0031-9201\(94\)90074-4](https://doi.org/10.1016/0031-9201(94)90074-4)
- Rowan, C. J., & Roberts, A. P. (2006). Magnetite dissolution, diachronous greigite formation, and secondary magnetizations from pyrite oxidation: Unravelling complex magnetizations in Neogene marine sediments from New Zealand. *Earth and Planetary Science Letters*, *241*(1–2), 119–137. <https://doi.org/10.1016/j.epsl.2005.10.017>
- Zhao, X., Heslop, D., & Roberts, A. P. (2015). A protocol for variable-resolution first-order reversal curve measurements. *Geochemistry, Geophysics, Geosystems*, *16*, 1364–1377. <https://doi.org/10.1002/2014GC005680>
- Zhao, X., Roberts, A. P., Heslop, D., Paterson, G. A., Li, Y., & Li, J. (2017). Magnetic domain state diagnosis using hysteresis reversal curves. *Journal of Geophysical Research: Solid Earth*, *122*, 4767–4789. <https://doi.org/10.1002/2016JB013683>